# PlenoptiCam v1.0: A light-field imaging framework

Christopher Hahne and Amar Aggoun
University of Wolverhampton, School of Mathematics and Computer Science
Wulfruna Street, WV1 1LY Wolverhampton, United Kingdom
{c.hahne, a.aggoun}@wlv.ac.uk

Abstract-Light-field cameras play a vital role for rich 3-D information retrieval in narrow range depth sensing applications. The key obstacle in composing light-fields from exposures taken by a plenoptic camera is to computationally calibrate, re-align and rearrange four-dimensional image data. Several attempts have been proposed to enhance the overall image quality by tailoring pipelines dedicated to particular plenoptic cameras and improving the color consistency across viewpoints at the expense of high computational loads. The framework presented herein advances prior outcomes thanks to its cost-effective color equalization from parallax-invariant probability distribution transfers and a novel micro image scale-space analysis for generic camera calibration independent of the lens specifications. Our framework compensates for artifacts from the sensor and micro lens grid in an innovative way to enable superior quality in sub-aperture image extraction, computational refocusing and Scheimpflug rendering with sub-sampling capabilities. Benchmark comparisons using established image metrics suggest that our proposed pipeline outperforms state-of-the-art tool chains in the majority of cases. The algorithms described in this paper are released under an open-source license, offer cross-platform compatibility with few dependencies and a graphical user interface. This makes the reproduction of results and experimentation with plenoptic camera technology convenient for peer researchers, developers, photographers, data scientists and others working in this field.

Index Terms-plenoptic, light-field, calibration, color transfer

## I. INTRODUCTION

THERE is a growing body of literature in the fields of experimental photography [1], [2], medical imaging [3], [4], [5], [6] and machine learning [7] recognizing capabilities offered by light-fields.

## A. Background

The probably most influential light-field model in computer graphics was devised by Levoy and Hanrahan [8] who described a light-field to be a collection of ray vectors piercing through two planes stacked behind one another. The intersections of ray vectors at the two planes make up four Cartesian coordinates, which is why light-fields are often referred to as four-dimensional (4-D). In their much celebrated paper, Levoy and Hanrahan demonstrate that the two planes serve as the spatial and angular image domain providing two different light-field representations that can be transferred into each other. Such light-field transformation corresponds to changing the sequential order of the two planes.

Capturing a light-field from a monocular lens is achieved with a single sensor stacked behind an aperture grid [9] such as a Micro Lens Array (MLA). This optical setup is known as

a plenoptic camera and can be thought of as accommodating an array of consistently spaced virtual cameras located at the aperture plane [10]. As opposed to light-fields from a camera array, captures from the plenoptic camera need to undergo additional processing to be represented as such [11], [12].

Until today, the landscape of software tools treating plenoptic content has been characterized by heterogeneity. One of the most mature and influential software applications was released by camera manufacturer Lytro in 2012. Lytro's image processing pipeline remains closed-source and is not publicly maintained since the company shut down business in 2018. In the earlier days of Lytro's lifetime, independent programmers developed binary file decoders by reverse-engineering Lytro's file formats [13], [14]. These tools, however, are unable to perform light-field rendering functionalities such as refocusing. Several scientists published methods on how to algorithmically calibrate Lytro's plenoptic camera within Matlab [11], [12], [15]. These methods are based on the given metadata while concentrating on the micro image center detection, 4-D rearrangement and rectification of radial lens distortions. More recently, research has taken the direction to successfully recover physical information at light-field boundaries [16], [17]. Although these studies revealed convincing results, lightfield color consistency as proposed by Matysiak et al. [17] requires high computational resources.

# B. Novelties

While consolidating preliminary decoding procedures, we introduce innovative calibration, resampling, color management and refocusing techniques in a cost-effective manner. An overview of our contributions is listed below:

- Scale space analysis of micro images is conducted early in the calibration pipeline to support plenoptic cameras with arbitrary sensor and MLA dimensions and, unlike other methods in the field, handle footage from custombuilt prototypes as well as Lytro cameras.
- Centroid grid fitting is employed using the Levenberg-Marquardt optimization to reduce least-squares errors of detected micro lens centers globally and determine the centroid spacing and rotation angle simultaneously.
- De-vignetting is based on a 4-D white image leastsquares fit model to suppress noise propagation as it occurs in a conventional white image division.
- 4) To counteract color variances across sub-aperture views, we propose a novel, rapid and effective illumination channel correction scheme.

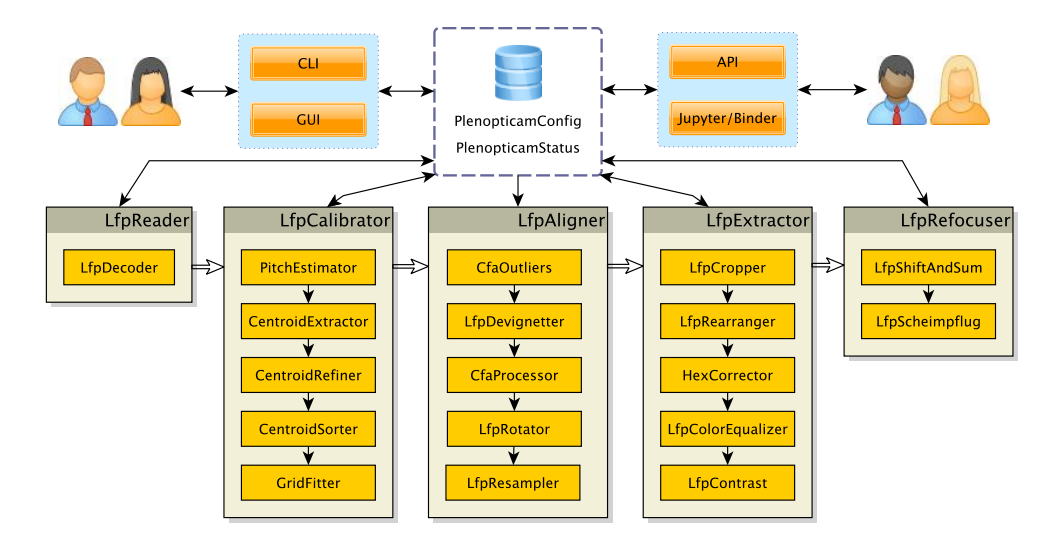


Fig. 1: Package architecture with gray blocks representing modules whereas orange blocks indicate essential top-level classes.

- 5) For accurate angular sampling, we offer micro image resampling followed by a hexagonal artifact removal.
- 6) Taking advantage of the popular computational refocusing, we pave the way for its Scheimpflug equivalent.

These innovations help leverage PLENOPTICAM to accomplish outstanding results, which are validated in this study with standard image metrics.

#### C. Scope

Equipped with generic calibration, decoding and rendering routines, PLENOPTICAM may build the foundation for future research on light-field image algorithms. Novel research goals can be achieved more easily as image scientists can adapt code and focus on their individual idea. The absence of powerful and heavy-weight libraries is intended to keep the dependency list short. Nonetheless, additional libraries can be used as an extension, e.g. to rectify lens distortions and extract depth at a post-processing stage. Note that PLENOPTICAM can be used in conjunction with the geometry tool PLENOPTISIGN [18] to pinpoint metric object positions in a light-field captured by a plenoptic camera.

# D. Structure of the Paper

The organisation of this paper begins with an introduction to the architectural design of the modules covering novel algorithms, which can be regarded as a roadmap for Section II. Subsections contained in Section II then give insightful details on algorithmic aspects with respect to plenoptic image calibration, sub-aperture extraction and refocusing. A benchmark comparison of results rendered by PLENOPTICAM and other tool chains is carried out in Section III. Section IV draws conclusions, while reflecting on the framework's potential impact and sketching out ideas for future work.

## II. MODULE FUNCTIONALITIES

An architectural scheme of the processing pipeline is sketched in Fig. 1. Objects of a PLENOPTICAMCONFIG and

PLENOPTICAMSTATUS class are thought to be singletons and shared across modules. The processing direction of input image data is from left to right (on module-level) and top to bottom (on class-level) as indicated by the arrows. The diagram in Fig. 1 can be regarded as a roadmap for this section in which the core functionality of each module is presented.

## A. LfpReader

The LFPREADER module supports standard image file types (tiff, bmp, jpg, png) and the more specific raw Lytro file type decoding (lfp, lfr, raw) for Bayer image composition according to the findings by Nirav Patel [13]. For raw data from a Lytro camera, this module exports an image as a tiff file in Bayer representation as well as a json file containing corresponding metadata which is used for gamma correction. Other image file types are expected to be in sRGB space for gamma handling.

#### B. LfpCalibrator

The fundamental problem we aim to solve when calibrating a plenoptic camera is to register geometric properties of the 4-D micro image representation. This enables a light-field to be rearranged as if captured by an array of multiple cameras with consistent spacing [10]. PLENOPTICAM introduces a novel and generic plenoptic image calibration pipeline with a sequence of steps shown in Fig. 2.

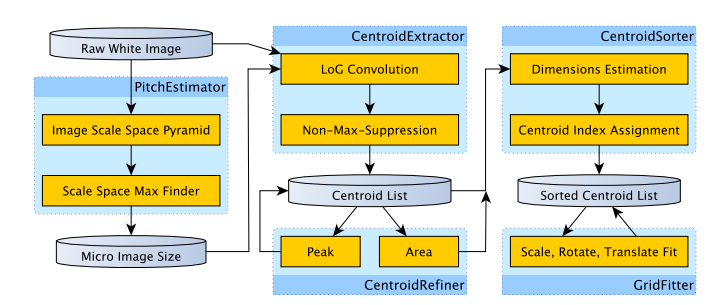


Fig. 2: Calibration pipeline

The entire procedure can be sub-divided into pitch estimation, centroid extraction along with optional refinements and centroid sorting of present micro images. To let the pipeline cover multiple types of plenoptic cameras with varying lens and sensor specifications, a blob detector is employed as a first step for analysis of the micro image size.

1) PitchEstimator: Based on a white calibration image  $I_w(\mathbf{x})$  with arbitrary micro images, we adapt the classical scale space theory [19] for optimized performance using half-octave pyramids [20] denoted by  $P(\nu, \mathbf{x})$  and built via

$$\forall \nu, \ P(\nu+1, \mathbf{x}) = \mathcal{D}_2 \left( P(\nu, \mathbf{x}) * \nabla^2 G(\sigma, \mathbf{x}) \right) \tag{1}$$

where  $\{\nu \in \mathbb{N} \mid \nu < \log_2\left(\min(K,L)\right)\}$  and K,L are spatial resolutions of  $I_w(\mathbf{x})$ . Downsampling is represented by  $\mathcal{D}_2(\cdot)$  considering the half-octave requirement and  $\nabla^2 G(\sigma,\mathbf{x})$  is the Laplacian of Gaussian (LoG) convolution kernel, known as the Mexican hat, which is approximated by the Difference of Gaussians. Each pyramid level at index  $\nu$  is then a downscaled LoG-filtered version of the previous level where  $P(0,\mathbf{x}) = I_w(\mathbf{x}) * \nabla^2 G(\sigma,\mathbf{x})$  serves as the initial scale. Let  $\nu^*$  be the level exhibiting the maximum intensity across all  $\nu$  given by

$$\nu^{\star} = \arg\max_{\nu} \left\{ \max_{\mathbf{x}} P(\nu, \mathbf{x}) \right\}, \qquad (2)$$

we infer  $\sigma^*$  as the detected blob radius at the initial scale by

$$\sigma^* = 2^{\nu^*/2} \sqrt{2^{\operatorname{mod}(\nu^*,2)}} \tag{3}$$

where the base-2 terms account for halved resolutions and the half-octave representation across pyramid levels, respectively. It may be an intuitive observation that a diameter M of a micro image proportionally scales with the blob radius  $\sigma^{\star}$ . A proof for this relationship is provided in Appendix A. Section III-A demonstrates that our automatic detection of the micro image size M is an important feature for micro image registration and subsequent light-field alignment processes, which enable PLENOPTICAM to cope with a variety of different MLA and objective lens specifications.

2) CentroidExtractor: Initial approximation of Micro Image Centers (MICs) is a key task in plenoptic image registration and has been subject of existing research. An early method developed by Dansereau et al. [12] convolves a white image from a Lytro camera with a dedicated kernel of constant size and subsequently analyzes local peaks. Cho et al. [11] and similarly Liang et al. [21] iteratively apply a morphological erosion operator to white images until a pattern of isolated micro image regions is obtained. Although image erosion facilitates rough centroid detection from intensity maxima, the iterative nature of this approach leaves space for optimizations with regards to speed and robustness. Unlike the previous detection methods, we identify MICs as local extrema in a LoG-convoluted image  $I_c(\mathbf{x}) = I_w(\mathbf{x}) * \nabla^2 G(\sigma^*, \mathbf{x})$  by using Non-Maximum-Suppression (NMS) in the form of the  $3 \times 3$ neighborhood scan. Here the kernel  $\nabla^2 G(\sigma^*, \mathbf{x})$  scales with M and helps carve out micro image peaks as it is responsive to the detected feature size. The vector  $\mathbf{x} = \{k, l\} \in \mathbb{Z}^2$ consists of image coordinates k, l for the two spatial directions, respectively. We obtain each MIC denoted as  $\mathbf{c} = \{k, l\} \in \mathbb{Z}^2$ by employing Pham's NMS method [22].

3) CentroidRefiner: It is important to note that the preliminary CENTROIDEXTRACTOR yields centroids located at integer sensor coordinates. Several studies have shown that integer coordinate precision induces artifacts when decomposing a raw plenoptic image to the sub-aperture image representation of a light-field [11], [12], [21]. For accurate light-field decomposition, we refine centroids with sub-pixel precision by taking pixel intensities into account that belong to the same micro image region  $\mathcal{R}$ , which is typically in a range of  $M \times M$  size. To obtain sub-pixel precise centroids  $\bar{\mathbf{c}} = \{\bar{k}, \bar{l}\} \in \mathbb{R}^2$ , we perform coordinate refinement by

$$\bar{k} = \sum_{(k,l) \in \mathcal{R}} \frac{I_c(k,l) \cdot k}{\sum I_c(k,l)} \quad \text{and} \quad \bar{l} = \sum_{(k,l) \in \mathcal{R}} \frac{I_c(k,l) \cdot l}{\sum I_c(k,l)} \quad (4)$$

where  $I_c(k,l)$  represents a LoG-convoluted white image. As an alternative, we compute area centroids from a binary micro image after thresholding with the 75th percentile of  $I_c(k,l)$  which then simplifies Eq. (4) to

$$\bar{k} = \frac{1}{|\mathcal{R}|} \sum_{(k,l) \in \mathcal{R}} k \quad \text{and} \quad \bar{l} = \frac{1}{|\mathcal{R}|} \sum_{(k,l) \in \mathcal{R}} l$$
 (5)

where  $|\cdot|$  denotes the cardinality providing the total number of elements within a micro image region  $\mathcal{R}$  above the threshold value. By default, PLENOPTICAM uses the latter approach given in Eq. (5) as it proves to be the more generic solution for white images suffering from noise or saturation. Figures 5 and 14 show examples of detected centroids using this method.

4) CentroidSorter: Let  $\mathbf{C} = \{\bar{\mathbf{c}}_p \mid p \in \mathbb{N}\}$  be a finite and unordered set of MIC coordinates  $\bar{\mathbf{c}}_p = \{\bar{k}, \bar{l}\}$ , little is known about the dimensions and geometric arrangement of the micro lenses. To enable generic calibration for different plenoptic camera models, it is necessary to examine fundamental properties of a custom MLA with arbitrary dimensions. For a first centroid spacing approximation, we assume the ratio of sensor dimensions K and L matches the aspect ratio of the MLA giving  $H = \sqrt{|\mathbf{C}| \times L/K}$  for the horizontal micro lens resolution with  $|\mathbf{C}|$  as the total number of centroids. The centroid spacing is estimated via L/H and used to form a set of neighbours  $\mathbf{S}$  from an arbitrary centroid  $\bar{\mathbf{c}}_r \in \mathbf{C}$  via

$$\mathbf{S} = \{ \bar{\mathbf{c}}_p - \bar{\mathbf{c}}_r \mid \bar{\mathbf{c}}_p \in \mathbf{C} \land L/2H < \|\bar{\mathbf{c}}_p - \bar{\mathbf{c}}_r\|_2 < 3L/2H \}$$
 (6)

where  $\|\cdot\|_2$  denotes the  $\ell^2$  norm. The MLA packing geometry  $\mathcal{P}$  is determined by analyzing angles of  $\bar{\mathbf{c}}_p \in \mathbf{S}$  as follows

$$\mathcal{P} := \begin{cases} \text{hexagonal,} & \text{if } \forall \bar{\mathbf{c}}_p \in \mathbf{S}, \lfloor \alpha(\bar{\mathbf{c}}_p)^{12}/\pi \rceil \in \{1, 3\} \\ \text{rectangular,} & \text{if } \forall \bar{\mathbf{c}}_p \in \mathbf{S}, \lfloor \alpha(\bar{\mathbf{c}}_p)^{12}/\pi \rceil \in \{0, 3\} \end{cases}$$
(7)

where  $\lfloor \cdot \rfloor$  is the nearest integer operation and an angle  $\alpha(\bar{\mathbf{c}}_p)$  is obtained using the inner product  $\langle \cdot, \cdot \rangle$  by

$$\alpha(\bar{\mathbf{c}}_p) = \arccos\left(\left\langle \frac{\left(\mid \bar{k}_p\mid,\mid \bar{l}_p\mid\right)}{\parallel \bar{\mathbf{c}}_p\parallel}, \frac{(1,1)}{\parallel (1,1)\parallel}\right\rangle\right) \tag{8}$$

Note that for a rectangular MLA packing, centroid spacings tend to be equal, but deviate by a factor of  $\sqrt{3}/2$  in the hexagonal case as illustrated in Fig. 3(b).

Rearranging plenoptic micro images to sub-aperture representation requires centroids to be indexed since their relative positions act as spatial coordinates in the sub-aperture image domain. At this point, however, the order of centroids within the array remains ambiguous. Thus, we seek a procedure that assigns indices  $j \in \{1, 2, \ldots, J\}$  and  $h \in \{1, 2, \ldots, H\}$  to each micro image centroid  $\bar{\mathbf{c}}_{j,h}$ . The proposed sort procedure begins with the search for the most upper left centroid  $\bar{\mathbf{c}}_{1,1}$  with j=1, h=1 which is found by the minimum Euclidean distance to the image origin as given by

$$\bar{\mathbf{c}}_{1,1} = \bar{\mathbf{c}}_{p^{\star}}, \quad \text{where} \quad p^{\star} \in \underset{1 \le p \le |\mathbf{C}|}{\min} (\|\bar{\mathbf{c}}_p\|_2)$$
 (9)

On the basis of an indexed centroid  $\bar{\mathbf{c}}_{j,h}$ , we search for its spatial neighbor by iterating through  $\mathbf{C}$  until finding a candidate  $\bar{\mathbf{c}}_{v} = \{\bar{k}, \bar{l}\}$  as seen in

$$\bar{\mathbf{c}}_{j+1,h} = \{ \bar{\mathbf{c}}_p \mid \bar{\mathbf{c}}_p \in \mathbf{C} \land \varphi(\bar{\mathbf{c}}_{j,h}, \bar{\mathbf{c}}_p) \}$$
(10)

that satisfies a boundary condition  $\varphi(\cdot) \in \{0,1\}$  given by

$$\varphi(\bar{\mathbf{c}}_a, \bar{\mathbf{c}}_b) = \bar{k}_a + \Upsilon_1 < \bar{k}_b < \bar{k}_a + \Upsilon_2 \land \bar{l}_a + \Upsilon_3 < \bar{l}_b < \bar{l}_a + \Upsilon_4$$
(11)

where  $\Upsilon = \mathbf{e}^M/2$  with  $\mathbf{e} = \{e_1, e_2, e_3, e_4\}$  is a boundary scale parameter set considering the micro lens packing geometry. Boundary parameters thus rely on a previously determined MLA structure and its micro image size M. Note that  $\bar{k}$  and  $\bar{l}$  may be swapped in Eq. (11) to switch between horizontal and vertical search directions. An exemplary result showing indexed centroids is depicted in Fig. 5.

5) GridFitter: At this stage of the calibration pipeline, centroids rely on intensity distributions, which may be affected by a broad range of irregularities arising from the MLA-sensor compound. Dansereau *et al.* [12] compress centroid information by forming a consistently spaced grid based on provided metadata. Usage of Delaunay triangulation as proposed by Cho *et al.* [11] suits hexagonal arrangements, but lacks to compensate for grid inconsistencies. Instead, we elaborate on a least-squares (LSQ) regression as potentially intended in a patent by Lytro [21].

For the fitting, we formulate an objective vector function  $\mathbf{f}=F(\cdot)$  using a grid generating model  $G(\cdot)$  and the detected centroids  $\bar{\mathbf{c}}_{i,h}$  as follows

$$\mathbf{f} = F(\mathbf{p}; J, H, \mathcal{P}, \bar{\mathbf{c}}_{i,h}) = \|\bar{\mathbf{c}}_{i,h} - G(\mathbf{p}; J, H, \mathcal{P})\|_2 \quad (12)$$

where  $\mathbf{p} = [c_y, c_x, s_y, s_x, \theta]$  consists of spatial center offsets  $(c_y, c_x)$ , grid scales  $(s_y, s_x)$  and a rotation angle  $\theta$  being subject to optimization. The micro lens numbers (J, H) and packing geometry  $\mathcal P$  are previously determined constants. Let the Levenberg-Marquardt (LM) step be given by

$$\mathbf{p}_{k+1} = \mathbf{p}_k - (\mathbf{J}^{\mathsf{T}}\mathbf{J} + \mu \mathbf{D}^{\mathsf{T}}\mathbf{D})^{-1}\mathbf{J}^{\mathsf{T}}\mathbf{f}$$
(13)

where  $\bf J$  is the Jacobian,  $\bf J^{\intercal} \bf J$  represents the Hessian approximate with  $^{\intercal}$  as the matrix transpose and  $\bf J^{\intercal} \bf f$  acts as the gradient [23]. Here, a diagonal matrix  $\bf D$  with damping term  $\mu$  allows for fast LM convergence. As opposed to an analytically derived Jacobian  $\bf J$ , a multi-variate numerical approximate  $\tilde{\bf J}({\bf p}) \approx {\bf J}$  is employed. The iterative update procedure proceeds until a convergence condition is met. Successful estimates  ${\bf p}^{\star}$  are fed into the grid model for a final centroid reassignment  $\bar{\bf c}_{j,h} := G({\bf p}^{\star}; J, H, \mathcal{P})$ . Enhancements of the herein proposed LSQ grid fit are examined in Section III-A.

C. LfpAligner

1) CfaOutliers: Often, hot and dead pixels arise from electrical response variations in the sensor hardware and become noticeable as intensity outliers. In contrast to other pipelines [12], [17], we detect and rectify outliers prior to demosaicing channels from the Color Filter Array (CFA). The reasoning behind our decision is that false intensities are propagated to adjacent pixels during demosaicing, which may pass unnoticed by a detection at a later processing stage. To identify outliers, we regard each of the four Bayer channels as a two-dimensional (2-D) grey scale image  $I_B(\mathbf{x})$  and analyze the difference from its Median-filtered version given by

$$I_R(\mathbf{x}) = I_B(\mathbf{x}) - \mathcal{M}(I_B(\mathbf{x})) \tag{14}$$

where  $I_R(\mathbf{x})$  is the reference image used for further analysis and  $\mathcal{M}(\cdot)$  denotes the Median filter operator. From  $I_R(\mathbf{x})$ , we obtain the arithmetic mean  $\bar{I}_R$  and the standard deviation  $\sigma$  as local statistical measures from a sliding window of 2n+1 size to replace potential outliers  $I_B(\mathbf{x})$  as follows

$$I_B(\mathbf{x}) = \begin{cases} \mathcal{M}(I_B(\mathbf{x})), & \text{if } I_B(\mathbf{x}) > \bar{I}_R + 4\sigma \\ I_B(\mathbf{x}), & \text{otherwise} \end{cases}$$
 (15)

where the if clause statement helps detect intensity outliers. Once a condition is fulfilled, nearby intensities in the range of 2n+1 are used to replace an outlier. The selection is further constrained by only accepting a small number n of candidates in a  $n^2 \times n^2$  window. Without this constrain, many pixels of a saturated image area would be falsely detected as outliers.

2) LfpDevignetter: In optical imaging, vignetting occurs at non-paraxial image areas as a result of either mechanical blocking of light rays or illumination fall-off from the cosine-fourth law, which arise from the Lambertian reflectance, pupil size reduction and the distance-dependant inverse square law [24]. Images from a plenoptic camera suffer from vignetting in similar ways whereas the appearance is given in 4-D representation. This image artifact may be treated through a pixel-wise division of the normalized white calibration image [12], [17]. PLENOPTICAM uses this method by default, as it works sufficiently well for white images not severely suffering from noise.

To reduce potential sensor noise, LFPDEVIGNETTER offers an alternative approach to counteract vignetting based on LSQ fitting which is traditionally used in 2-D image processing. The LSQ de-vignetting principle, however, has not yet been applied to raw images of a plenoptic camera. We adapt the classical procedure by iterating through each micro image and performing rectification via division of normalized LSQ fit values to prevent further propagation of noise to the light-field.

The intensity surface of a white micro image  $I_m(u,v)$  is approximated by a multivariate polynomial regression. For  $2^{nd}$  order polynomials, this fit function may be given as

$$I_m(u,v) = w_1 + w_2 u + w_3 v + \ldots + w_7 u^2 v^2$$
 (16)

with  $\mathbf{w} = \begin{bmatrix} w_1 & w_2 & \dots & w_7 \end{bmatrix}^\mathsf{T}$  as the regression coefficients. Provided the 2-D micro image coordinate indices u and v, this is translated to matrix form by

$$\mathbf{A} = \begin{bmatrix} 1 & u_1 & v_1 & \cdots & u_1^2 v_1^2 \\ 1 & u_2 & v_2 & \cdots & u_1^2 v_2^2 \\ \vdots & \vdots & \vdots & \ddots & \vdots \\ 1 & u_M & v_M & \cdots & u_M^2 v_M^2 \end{bmatrix}, \, \mathbf{b} = \begin{bmatrix} I_m(u_1, v_1) \\ I_m(u_1, v_2) \\ \vdots \\ I_m(u_M, v_M) \end{bmatrix}$$
(17)

with  $\bf A$  as Vandermonde matrix and vector  $\bf b$  containing micro image intensities. As  $\bf A$  is generally non-square, the equation system is solved via the Moore-Penrose pseudo-inverse denoted as  $^+$  and given by

$$\mathbf{A}^{+} = (\mathbf{A}^{\mathsf{T}} \, \mathbf{A})^{-1} \, \mathbf{A}^{\mathsf{T}} \tag{18}$$

so that we obtain fit values w for each micro image by

$$\mathbf{w} = \mathbf{A}^{+}\mathbf{b} \tag{19}$$

After estimation of weight coefficients, we divide each micro image of the light field by its fitted counterpart from the white calibration image. The herein described method is left optional due to the comparably extensive computational requirements. Its effectiveness is demonstrated in Section III-C.

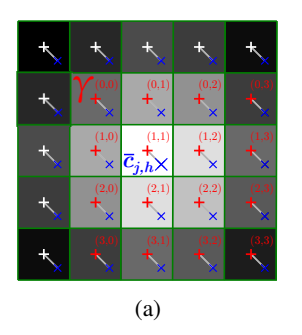
- 3) CfaProcessor: The CFAPROCESSOR class is dedicated to raw sensor images and can be useful for processing Lytro binary file data for which the featured metadata is considered. Regardless of the file type, the CFAPROCESSOR takes care of debayering, white balancing just as color correction. By default, Menon's algorithm [25] is employed for debayering from the available COLOUR\_DEMOSAICING implementation. Findings made by CLIM-VSENSE with regards to highlight processing were adopted by this class as they yield enhanced sub-aperture image quality.
- 4) LfpRotator: At the assembling stage of a plenoptic camera, a micro lens grid is ideally placed so that its tilt angles are in line with that of a sensor array. In the real world, however, this grid may likely be displaced with respect to the pixel grid. We suppose that the sensor and MLA planes can be considered parallel by mechanical design, where the back focal plane of a plano-convex MLA coincides with the sensor's image plane once its cover glass touches the planar back vertex of an MLA. To counteract rotations about the z axis, our approach exploits the fact that images exposing aberrations tend to be aberration-free along their central axes. This suggests that a centroid row close to the image center forms a line, which may be a reliable indicator for the MLA rotation angle. Such a central row  $\bar{\mathbf{c}}_{j,\delta} = \{\bar{k}_{j,\delta}, \bar{l}_{j,\delta}\}$  is obtained by  $\delta := \lfloor (H-1)/2 \rfloor$ with H as the total number of micro lenses in the vertical direction. Applying LSQ regression on  $\bar{\mathbf{c}}_{i,\delta}$  similar to Eqs. (12) and (13) yields the angle  $\theta$ . Centroid and image rotation is accomplished by successively multiplying coordinates with a rotation matrix  $\mathbf{R}_{\theta}$  and a translation matrix  $\mathbf{T}$  giving a new centroid set  $\bar{\mathbf{c}}'_{j,h} = \mathbf{T}^{-1} \mathbf{R}_{\theta} \mathbf{T} \bar{\mathbf{c}}_{j,h}$ . An example showing results of the proposed procedure is provided in Fig. 14.
- 5) LfpResampler: Section II-B reveals that micro image centroids  $\bar{\mathbf{c}}_{j,h} \in \mathbb{R}^2$  are likely to be found at sub-pixel positions. Taking pixel intensities from nearest integer coordinates

leads to errors and thus image artifacts [11]. It is mandatory to preserve fractional digits of MIC coordinates to accurately decompose a light-field from a plenoptic camera. Therefore, we introduce an interpolation scheme, which retains accuracy by resampling each micro image  $I_m(u,v)$  individually.

Figure 3(a) depicts an MIC  $\bar{\mathbf{c}}_{j,h}$  and the corresponding bi-cubic coefficients  $\gamma$  based on surrounding pixel centers indexed by (i,j). Given  $\gamma_{i,j}$  as pre-determined weighting coefficients, the sub-pixel precise illuminance surface  $A(\cdot)$  at each centroid  $\bar{\mathbf{c}}_{j,h} = \{\bar{u}_{j,h}, \bar{v}_{j,h}\} \in \mathbb{R}^2$  is computed via

$$A(u,v) = \sum_{i=1}^{4} \sum_{j=1}^{4} \gamma_{i,j} \cdot u^{i-1} \cdot v^{j-1}$$
 (20)

where u,v are indices in the  $4\times 4$  image pixel patch and  $\bar{\mathbf{c}}_{j,h} = \{\bar{u}_{j,h}, \bar{v}_{j,h}\} \in \mathbb{R}^2$  denote the coordinates of the centroid at which the intensity is interpolated.



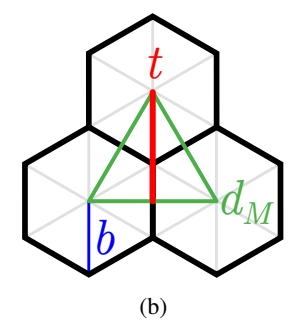


Fig. 3: **Interpolation schemes** with (a) micro image centering and (b) MIC geometry in a hexagonal grid with t as the height and  $d_M$  as the side length of an isosceles triangle.

Apart from handling rectangular MLA grids, LFPRESAM-PLER supports rectification of a hexagonal micro lens arrangement, which is detected by Eq. (7) prior to the sort procedure. In the hexagonal case, the alignment is accomplished by deinterleaving and elongating one dimension at the resampling stage. This shift and stretch is required as a consequence of the hexagonal geometry depicted in Fig. 3(b) and involves onedimensional upsampling of the effective resolution. We obtain the height of a triangle spanned by three MICs with t = 3b/2and its side length by  $d_M = b\sqrt{3}$  which represents the spacing of two MICs as in a rectangular grid. From this, it follows that the sampling density along t is  $2/\sqrt{3}$  times higher in relation to  $d_M$ . One may note that  $d_M/t = \sqrt{3}/3/2$  becomes  $2/\sqrt{3}$ after rearranging. Further, it is seen that hexagonal packings imply a displacement of  $d_M/2$  for every second MIC coordinate vector. Thus, rectification of honeycomb structures may be achieved by translating every other coordinate vector by  $d_M/2$ and simultaneously interpolating the number of micro images by factor  $2/\sqrt{3}$  along the direction orthogonal to t, which corresponds to the horizontal dimension in Lytro cameras.

#### D. LfpExtractor

1) LfpRearranger: Let  $E_{fs}[s_j,u_{c+i}]$  be a spatio-angular 2-D slice of an aligned 4-D micro image light-field and the rearrangement to a sub-aperture slice  $E_i[s_j]$  be given by

$$E_i[s_j] = E_{f_s}[s_j, u_{c+i}]$$
 (21)

where micro image pixels at  $u_{c+i}$  are consecutively collected and relocated in a new sub-aperture vector  $E_i[s_j]$ . After the alignment, each centroid is represented by the central position c=(M-1)/2 with mod(M,2)=1 from an odd micro image pixel diameter M. A change in index  $i\in\{-c,\ldots,c\}$  controls the relative viewpoint location in the light-field whereas index  $j\in\{1,2,\ldots,J\}$  iterates through micro lenses as the spatial domain. Note that Eq. (21) refers to one direction, which is equally applied orthogonal to it for complete rendering.

2) HexCorrector: While a hexagonal micro lens lattice increases the packing density and thus the spatial resolution, it causes a shortcoming at the rectangular resampling stage, becoming visible as fringe patterns along straight object edges in sub-aperture images (see Fig. 10 for details). This is a result of resampling every other row by half the spacing such that actual object edge transitions may move to incorrect positions causing a visual zipper-like appearance. Peer scientists addressed this issue via barycentric interpolation [11], posterior demosaicing [26] and depth-guided resampling [27]. To tackle this artifact after the fact, it is essential to identify affected pixel candidates.

For an analytical detection, we compose two auxiliary images  $E[\hat{s}_j]$  and  $E[\check{s}_j]$  by de-interlacing, i.e. taking every other row, of a sub-aperture image  $E_i[s_j]$  where  $E[\hat{s}_j]$  represents unshifted pixel vectors and  $E_i[\check{s}_j]$  the shifted ones. Then we deduct unshifted pixels from their shifted counterparts via

$$\tilde{V}_i[\check{s}_j] = E_i[\check{s}_j] - E_i[\hat{s}_j] \tag{22}$$

to extract local variances in an image vector  $\tilde{V}_i[\check{s}_j]$  containing strong responses at edges parallel to the shift and stretch direction. To remove edges of real objects, we further subtract the magnitude of the partial derivative  $\partial_{\hat{s}} E_i[\hat{s}_j]$  by

$$\bar{V}_i[\check{s}_j] = |\tilde{V}_i[\check{s}_j]| - |\partial_{\hat{s}} E_i[\hat{s}_j]| \tag{23}$$

to leave real edges out of consideration. At this stage, we assume  $\bar{V}_i[\check{s}_j]$  to exhibit peaks for potential candidates which we isolate from noisy responses via thresholding with  $\tau$  by

$$V_i[\check{s}_j] = \begin{cases} 1, & \text{if } \bar{V}_i[\check{s}_j] > \tau \\ 0, & \text{otherwise} \end{cases}$$
 (24)

To further exclude false positives along the shift and stretch direction, we reject candidates not being part of a consecutive sequence of minimum length 4 in an unraveled vector  $V_i[\hat{s}_j]$ . This way it is ensured that treated areas have sufficient length to be visually recognized. Finally, the remaining candidates in  $V_i[\hat{s}_j]$  are used to make substitutions in  $E_i[s_j]$  by

$$E_{i}[s_{j}] = \begin{cases} \frac{1}{|\mathcal{R}|} \sum_{h \in \mathcal{R}} E_{i}[t_{h}], & \text{if } V_{i}[\check{s}_{j}] = 1\\ E_{i}[s_{j}], & \text{otherwise} \end{cases}$$
 (25)

for each  $j \in \{1, 2, ..., J\}$  and where  $t_h$  denotes the dimension orthogonal to  $s_j$  in a surrounding region  $\mathcal{R}$  of a 2-D subaperture image. The effectiveness of this solution is demonstrated in Fig. 10.

3) LfpColorEqualizer: Lens components generally expose a gradual intensity decline toward image edges caused by the cosine-fourth law [24]. With a micro image fully covered by the sensor, this illumination fall-off is spread across a relatively small group of Bayer pattern pixels that are merged during demosaicing. Visible intensity variances in off-axis sub-aperture views are thus a result of vignetting at the micro image level that we aim to rectify with the LFPCOLOREQUALIZER module. Recent research dealt with enhancing the consistency of light intensities across light-field views [17]. The idea behind this concept is to propagate trusted intensities from paraxial image areas that expose no severe image aberrations to sub-aperture images located at the edge of a light-field. It can thus be used in addition to de-vignetting by utilizing the information redundancy within the light-field. In a recent study, Gaussian Mixture Models (GMMs) were employed in conjunction with disparity correspondences computed at a preceding stage to reduce color inconsistencies [17]. However, the authors note that their procedure requires a high computational load (240 mins per light-field) due to the many steps involved.

To overcome this limitation, we introduce linear mappings based on probability distributions. A well known classical method in image processing to achieve this is formally known as Histogram Matching (HM). HM proves to be advantageous when applied to light-fields as it is invariant of the texture so that it preserves parallax information while requiring relatively little computational effort as opposed to iterative methods like k-means. Besides this method, we employ a recent advance in image color transfer that is based on the Monge-Kantorovich-Linearization (MKL). MKL has been introduced to the field of image processing by Pitié and Kokaram [28] to facilitate automatic color grading in media production. As of now, the Monge-Kantorovich principle has not been applied in the context of equalizing colors across light-field views from a plenoptic camera. Moreover, MKL appears to not have been combined with channel-wise HM. Due to the linearization of MKL using Multi-Variate Gaussian Distributions (MVGDs) and its combination with HM, we expect our novel HM-MKL compound to outperform the stand-alone HM and Pitié's pure MKL in terms of accuracy while largely reducing the computational complexity imposed by the alternative GMM method [17]. Mathematical details of our joint HM-MKL mechanism are presented hereafter.

Similar to other literature [29], we denote  $f(r_k)$  to be a Probability Density Function (PDF) with  $r_k$  as color channel intensities of a sub-aperture image  $E_i[s_i]$  given by

$$f(r_k) = \frac{\eta(r_k)}{JH}, \quad \forall k \in \{1, 2, \dots, \mathcal{L}\}.$$
 (26)

Here  $\eta(\cdot)$  yields the number of pixels with intensity level k where  $\mathcal{L}$  is the level maximum. The histogram is normalized by JH as the total pixel count of the sub-aperture image. From this we compute  $F(r_k)$  as the Cumulative Density Function (CDF) which is obtained using an auxiliary index  $\epsilon$  via

$$F(r_k) = \sum_{\epsilon=1}^k f(r_\epsilon), \quad \forall k \in \{1, 2, \dots, \mathcal{L}\}.$$
 (27)

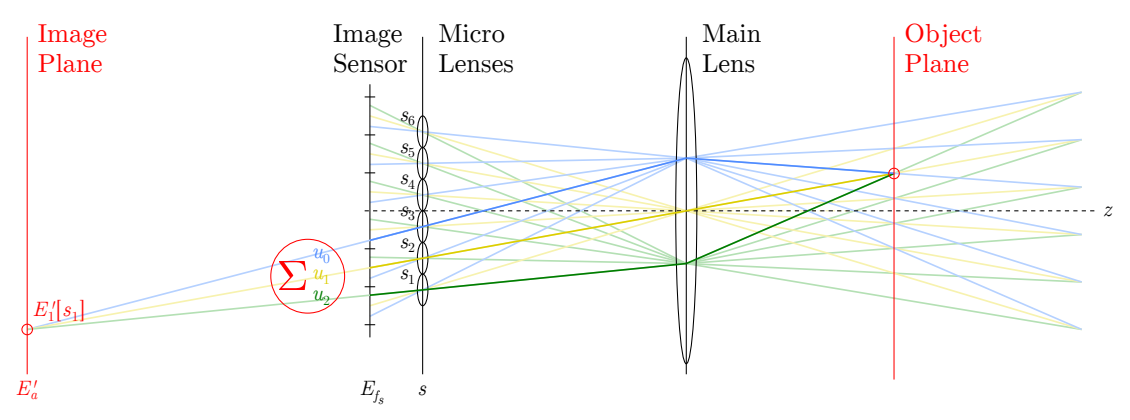


Fig. 4: **Refocusing concept** with chief ray intersections indicating object and image plane for a recovered point  $E'_1[s_1]$ .

To match the source  $F(r_k)$  with the target  $T(z_q)$ , we perform a pixel mapping via  $T^{-1}$  satisfying  $F(r_k) = T(z_q)$  such that

$$z_a = T^{-1}(F(r_k)) (28)$$

where each  $r_k$  gets assigned a new value  $z_q$  from the probability map  $T^{-1}$  implemented as a discrete lookup table.

While this channel-wise mapping is straightforward, it fails to sufficiently transfer color intensities at the level satisfying our human visual perception. It is thus our motivation to determine an optimal PDF transport plan. Due to the stochastic nature of intensities (r,g,b), we regard the source  $\mathbf{r} = \begin{bmatrix} r_k^{(r)}, r_k^{(g)}, r_k^{(b)} \end{bmatrix}^\mathsf{T}$  and target  $\mathbf{z} = \begin{bmatrix} z_q^{(r)}, z_q^{(g)}, z_q^{(b)} \end{bmatrix}^\mathsf{T}$  as correlated color channel MVGDs given by

$$\mathcal{N}(\mathbf{r}; \boldsymbol{\mu}_r, \boldsymbol{\Sigma}_r) = \frac{\exp\left(-\frac{1}{2}(\mathbf{r} - \boldsymbol{\mu}_r)^{\mathsf{T}} \boldsymbol{\Sigma}_r^{-1}(\mathbf{r} - \boldsymbol{\mu}_r)\right)}{\sqrt{(2\pi)^{\mathsf{rank}(\boldsymbol{\Sigma}_r)}|\boldsymbol{\Sigma}_r|}}$$
(29)

where  $\Sigma_r$  and  $\Sigma_z$  denote covariance matrices while  $\mu_r$  and  $\mu_z$  are the mean vectors of  $\mathbf{r}$  and  $\mathbf{z}$ , respectively. A desired transfer  $\hat{t}(\mathbf{z})$  requires the PDFs to be equal and thus fulfill the condition  $\mathcal{N}(\hat{t}(\mathbf{z}); \mu_z, \Sigma_z) \propto \mathcal{N}(\mathbf{r}; \mu_r, \Sigma_r)$ , which gives

$$(\mathbf{z} - \boldsymbol{\mu}_z)^{\intercal} \boldsymbol{\Sigma}_z^{-1} \left( \hat{t}(\mathbf{z}) - \boldsymbol{\mu}_z \right) = (\mathbf{r} - \boldsymbol{\mu}_r)^{\intercal} \boldsymbol{\Sigma}_r^{-1} (\mathbf{r} - \boldsymbol{\mu}_r) \quad (30)$$

after dropping the constant leading terms. Using the pseudo-inverse <sup>+</sup> as in Eq. (18), we arrange the above equation to

$$(\hat{t}(\mathbf{z}) - \boldsymbol{\mu}_z) = ((\mathbf{z} - \boldsymbol{\mu}_z)^{\mathsf{T}} \boldsymbol{\Sigma}_z^{-1})^+ (\mathbf{r} - \boldsymbol{\mu}_r)^{\mathsf{T}} \boldsymbol{\Sigma}_r^{-1} (\mathbf{r} - \boldsymbol{\mu}_r)$$
(31)

As we seek a compact transfer matrix, we define M to be

$$\mathbf{M} = \left( (\mathbf{z} - \boldsymbol{\mu}_z)^{\mathsf{T}} \boldsymbol{\Sigma}_z^{-1} \right)^+ (\mathbf{r} - \boldsymbol{\mu}_r)^{\mathsf{T}} \boldsymbol{\Sigma}_r^{-1}$$
 (32)

so that after substitution and rearranging, Eq. (31) becomes

$$\hat{t}(\mathbf{z}) = \mathbf{M}(\mathbf{r} - \boldsymbol{\mu}_r) + \boldsymbol{\mu}_z \tag{33}$$

for the forward transfer. The determination of  $\mathbf{M}$  is key for an optimal transport. We utilize Pitié's findings who employed MKL with  $\mathbf{M}^{\mathsf{T}} \mathbf{\Sigma}_z^{-1} \mathbf{M} = \mathbf{\Sigma}_r^{-1}$  and which is given by

$$\mathbf{M} = \mathbf{\Sigma}_r^{-1/2} \left( \mathbf{\Sigma}_r^{1/2} \mathbf{\Sigma}_z \mathbf{\Sigma}_r^{1/2} \right)^{1/2} \mathbf{\Sigma}_r^{-1/2}$$
 (34)

It is worth noting that Pitié elaborated on a variety of other solutions for M, e.g. Cholesky decomposition, among which MKL proved to be the most successful in terms of accuracy [30]. The implementation of the color equalization is

based on iterating through the 2-D angular light-field domain while taking the central image as a source **r** and each angular sample as **z**. An experimental evaluation of the proposed HM, MKL and HM-MKL methods is carried out in Section III.

## E. LfpRefocuser

The LFPREFOCUSER module enables computational change of the image focus based on light-field images. To achieve this, LFPREFOCUSER offers 3 different mechanisms on how to conduct refocusing. The fundamental technique is the conventional shift and sum method as originally presented by Isaksen *et al.* [31] who employed a light-field taken by an array of cameras. Transferring this concept to sub-aperture images  $E_i[s_j]$ , a refocused image vector  $E_a'[s_j]$  with synthetic focus parameter a is given by

$$E'_{a}[s_{j}] = \sum_{i=-c}^{c} E_{i}\left[s_{j-a(c+i)}\right], \quad a \in \mathbb{Q}$$
 (35)

for the 1-D case leaving out variables of the second spatial domain. A refinement option in PLENOPTICAM enables sub-pixel precision in refocusing via upsampling each sub-aperture image before integration. This not only increases the spatial resolution, but also allows for sub-sampling the refocused depth range along the optical axis of the main lens.

As an alternative to Eq. (35), shift and sum can be accomplished from an aligned micro image representation  $E_{f_s}[s_j, u_{c+i}]$  as a starting point, which then writes

$$E'_{a}[s_{j}] = \sum_{i=-c}^{c} E_{f_{s}}[s_{j+a(c-i)}, u_{c+i}], \quad a \in \mathbb{Q}$$
 (36)

and can be thought of as employing an interleaved convolution kernel as shown in our previous work examining FPGA-based refocusing practicability [32]. The concept behind Eq. (36) is illustrated in Fig. 4 with the aid of chief rays and paraxial optics for a more intuitive understanding of computational refocusing. Interested readers may note that refocused distances can be pinpointed in space, using this model [2], [18].

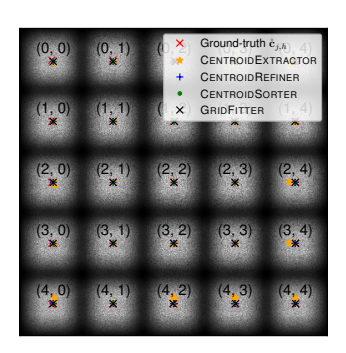
The refocuser module features the LFPSCHEIMPFLUG class which mimics the identically named principle on a computational level. Tilting the refocused plane is achieved through a fusion of spatial image areas from monotonically varying synthetic focus parameter a. This enables the LFPSCHEIMPFLUG

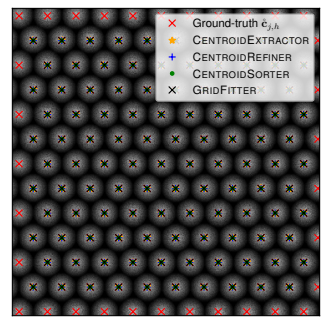
module to render tilted focus along horizontal, vertical and both diagonal image corner-to-corner directions, where focal start and end points rely on provided a. Figure 18 depicts a plenoptic-based photograph exhibiting the Scheimpflug effect.

#### III. RESULTS

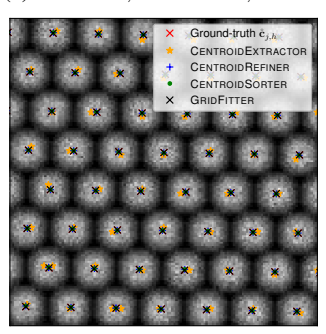
#### A. Calibration

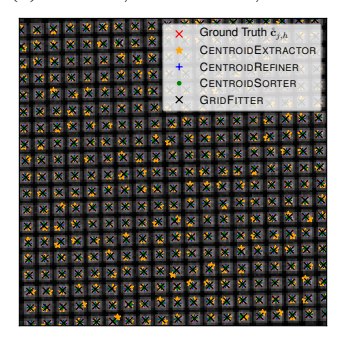
PLENOPTICAM's generic calibration capability is tested under different scenarios with micro images varying in size, number, rotation angle, packing geometry and pixel noise. Our proposed calibration pipeline is validated through synthesized data featuring respective ground-truth references. Results are depicted in Fig. 5 for visual inspection.





(a) M = 141, J = H = 5,  $\theta = 0^{\circ}$  (b) M = 52, J = H = 13,  $\theta = 0^{\circ}$ 





(c) 
$$M = 18$$
,  $J = H = 40$ ,  $\theta = 1^{\circ}$  (d)  $M = 8$ ,  $J = H = 90$ ,  $\theta = -2^{\circ}$ 

Fig. 5: **Auto-calibration results** from synthetic data showing noisy micro images varying in size with square pupil and rectangular packing in (a); circular pupil and hexagonal packing in (b); dense, tilted hexagonal packing in (c); and dense, tilted rectangular packing in (d).

To analyze the PITCHESTIMATOR as an early stage of the pipeline, scale space maxima along  $\nu$  are presented from the examples shown in Fig. 5(a) to (d).

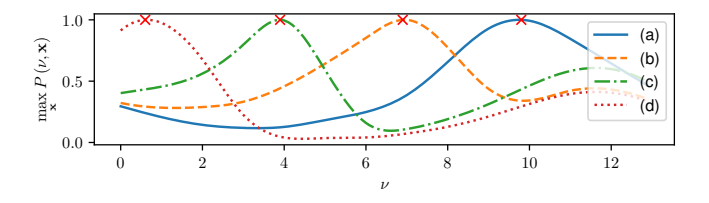


Fig. 6: Scale maxima analysis from PITCHESTIMATOR with pyramid data from Fig. 5 where crosses signify respective  $\nu^*$ 

For a quantitative examination of the centroid accuracy, we use C as a deviation metric in pixel unit given by

$$C = \frac{1}{JH} \sum_{j=1}^{J} \sum_{h=1}^{H} \| \mathbf{\hat{c}}_{j,h} - \bar{\mathbf{c}}_{j,h} \|_{2}$$
 (37)

for each of our centroid detection methods. Here  $\mathring{c}_{j,h}$  represents actual coordinates from the image synthesis that act as a ground-truth. Numerical results from Eq. (37) in Fig. 5 are provided in Table I. Figure 5(a) suggests that approximates from Centroidextractor appear significantly off with regards to the ground-truth while subsequent refinement stages enhance the accuracy. Closer inspection reveals that the Centroidextractor may yield several centroids for a micro image suffering from noise. This is a side effect of NMS which would have been of greater concern if white images were not convolved with  $\nabla^2 G(\sigma^*, \mathbf{x})$  prior to NMS, as this proves to cancel out false maxima. Candidates passing through Lfpextractor thus tend to be close to the ground-truth.

TABLE I: Centroid deviation C in [px]

T2:	Stage 1	Stage 2		Stage 3	Stage 4	Benchmark	
Fig.	CEN.	CEN.REFINER		CEN.	GRID	Dansereau	Schambach
3	EXTR.	peak	area	SORTER	FITTER	et al. [12]	et al. [33]
(a)	6.171	2.984	1.941	1.849	1.798	n.a.	n.a.
(b)	0.854	0.237	0.124	0.124	0.025	0.381	n.a.
(c)	1.741	0.667	0.167	0.166	0.011	0.261	1.121
(d)	0.896	0.419	0.293	0.289	0.008	n.a.	n.a.

From the results in Table I, it follows that the CENTROIDREFINER uses Eq. (5) by default as opposed to Eq. (4) which propagates more imprecise coordinates to subsequent procedures. The reason behind CENTROIDSORTER yielding better results in Table I is that it merges centroids belonging to the same micro image. Improvements of the GRIDFITTER arise from a large number of data points in the simultaneous parameter fit resulting in lower LSQ residuals. Despite this promising outcome, usage of GRIDFITTER is left optional to allow for calibration of inconsistent lattice spacing. One may note that mechanical vignetting causes off-center micro images to be of non-radially symmetric shape, shifting detected centers away from their actual physical counterparts. To work against this displacement, interested readers are referred to the methods proposed by peers [34], [21], [35], [33].

#### B. Sub-aperture images

The central view of a light-field generally suffers the least of aberrations and thus, exposes best image quality. Figure 8 depicts decoded central views of light-field photographs from the available IRISA dataset [36] rendered by state-of-the-art plenoptic imaging pipelines for comparison. Closer inspection reveals that central views from LFTOOLBOX V0.5 appear brighter, but - in contrast to the others - fail to preserve bright image details. For a quantitative assessment of the different pipelines, we seek a metric serving as an objective measure. Since central sub-aperture images lack ground-truth references, we employ a widely accepted no-reference-based technique named *Blind Reference-less Image Spatial Quality Evaluator* (BRISQUE) [37] from the *pybrisque* implementation [38]. Scores from the BRISQUE metric are presented in

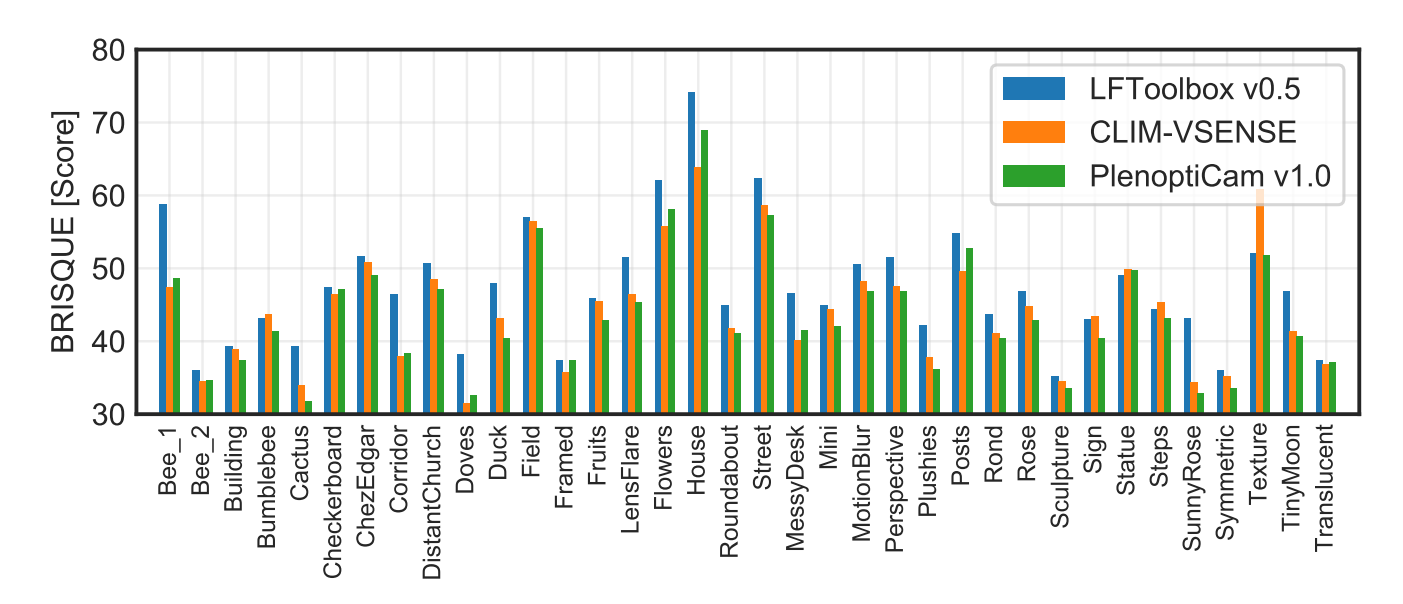


Fig. 7: Analysis of central sub-aperture images from [36] along the horizontal axis and BRISQUE metric scores along the vertical axis where lower values signify higher quality. Our tool chain outperforms others in 24 out of 36 images in total.

Fig. 7. Light-field denoising as borrowed by [17] was left out in the evaluation as it is considered equally effective for each pipeline and thus, not crucial for the decomposition. For our benchmark comparison, all pipelines are set to render with de-vignetting, color and sRGB options.

The BRISQUE metric is known to be sensitive to noise and blur by local statistical analysis so that an information loss caused by image processing modules would deteriorate the score. Low scores of our pipeline in Fig. 7 justify that on average our decomposition retains the physical information optimally. Our central sub-aperture images outperform the other two pipelines in 24 out of 36 cases of the dataset samples [36]. We achieve a total score of 1567 whereas CLIM-VSENSE yields 1595 and the LFTOOLBOX v0.5 gets 1702 scores. The reason for our strong results relies on our proposed extensions to existing pipelines. This includes the treatment of detected hot-pixels prior to Bayer demosaicing to prevent outliers from propagating to adjacent pixels. We further take advantage of Menon's method [25] for debayering. In addition, the LFPRESAMPLER contributes to lower scores by conducting micro image alignment in an element-wise manner instead of re-mapping the entire plenoptic image as a whole [39]. Another reason for the improvements is that PLENOPTICAM benefits from insights previously made available by peers such as the de-saturation approach [17]. Apart from that, our automatic dynamic range alignment based on percentiles of different color spaces tends to be a more generic solution for images of various exposure, which becomes apparent by comparing (h) with (i) in Fig. 8.

For comparisons with the Lytro engine, results were computed with LYTRO DESKTOP v3.4.4 and LYTRO POWER TOOLS v1.0. Thereby, metrics indicate that the latter yields brighter images with larger field of view and allows for numerical parametrization (e.g.  $\lambda$  for focus), making experimental reproduction easier. All Lytro results presented hereafter were

therefore generated using LYTRO POWER TOOLS V1.0.

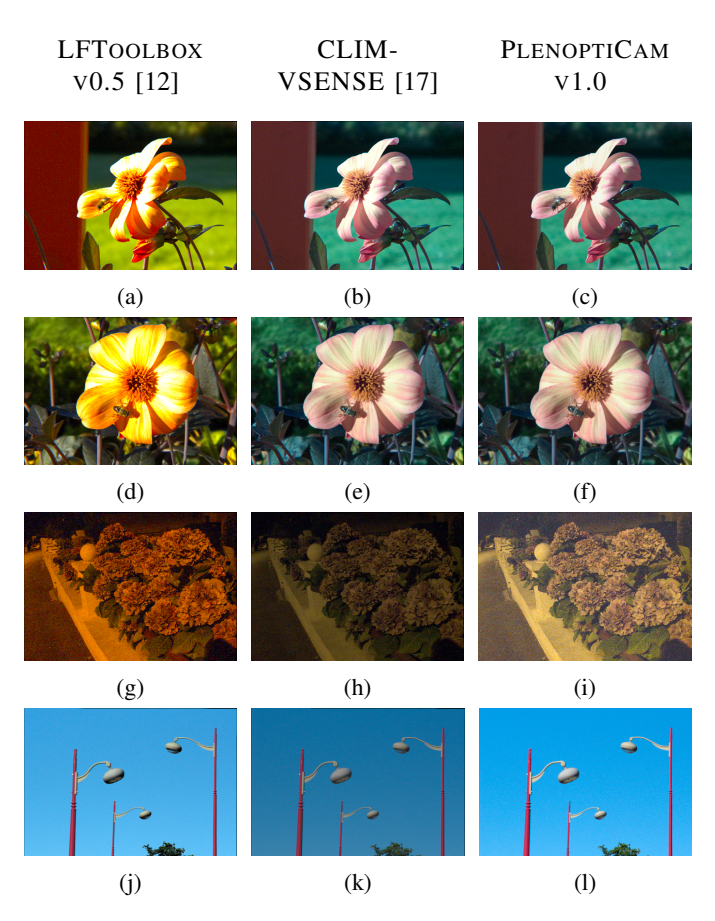


Fig. 8: **Central sub-aperture images** from the IRISA dataset [36] rendered by (left) LFTOOLBOX V0.5 [12], (middle) CLIM-VSENSE [17] and (right) ours for comparison.

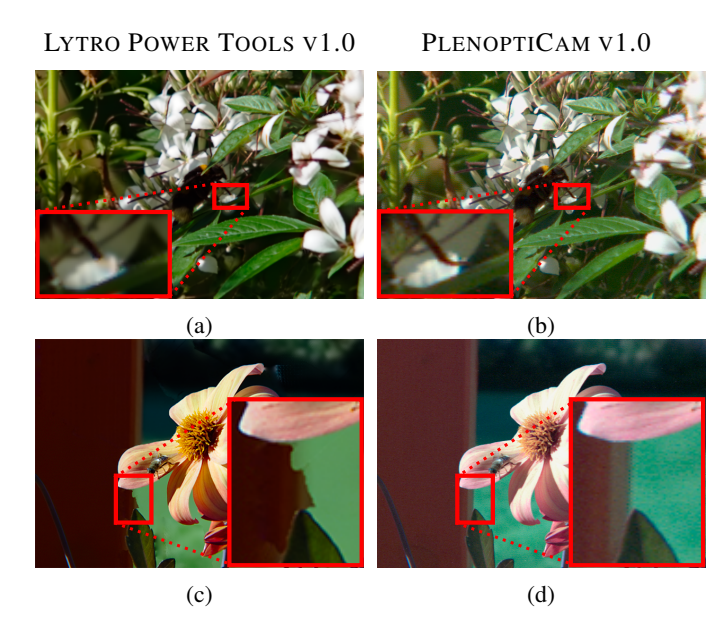


Fig. 9: **View comparison with Lytro engine** revealing differences between classical sub-aperture images (right column) and Lytro's results (left column), a consequence of all-in-focus rendering from depth-based segmentation [40], [41].

Figure 9 provides a comparison of light-field images rendered by Lytro Power Tools v1.0 and PlenoptiCam V1.0, respectively. On closer examination of the Lytro photographs in Figs. 9(a) and 9(c), occasional displacements emerge with image regions being removed or unnaturally shifted from their surroundings. Since Lytro's code has not been disclosed, the cause for this appearance can only be speculated. A study carried out by scientists formerly affiliated with Lytro suggests that a previously computed depth map is used to fuse a stack of high-resolution refocused frames to an all-in-focus image [40], [41], which in turn may be a starting point for high-resolution angular view synthesis. While this yields higher resolutions, unknown or erroneous disparity is propagated to subsequent stages, i.e. super-resolved views. Image region displacements in Figs. 9(a) and 9(c) thus might be due to false disparities in the depth map. Lytro's image resolutions are numerically higher than the number of present micro lenses, further supporting the assumption of such pipeline design. These observations bring us to the conclusion that the Lytro engine omits direct access to classical sub-aperture images unlike other available opensource toolchains [12], [17] including ours.

Technically, the user can generate sub-aperture images from Lytro's aligned ESLF images by completing their processing manually, including pixel rearrangements, adapting angular view positions and accounting for gamma as well as color correction. Given that those ESLF images are at a different processing stage and require additional resources, we compare PLENOPTICAM's sub-aperture images with the scientific toolbox [12] and its extensions [17]. Nonetheless, we then contrast our refocusing results against those of the Lytro engine in Section II-E.

For further sub-aperture image analysis, we focus on the results of the HEXCORRECTOR where artifacts caused by

hexagonal sampling are subject to removal. Figure 10 shows

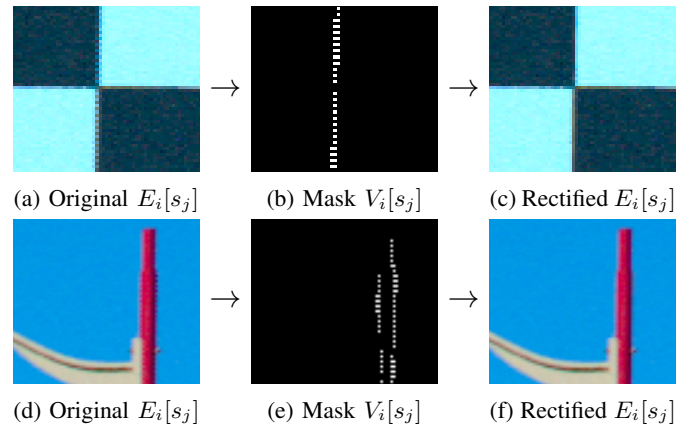


Fig. 10: Fringe artifact reduction results showing untreated sub-aperture images in the left column, exhibiting fringes along vertical lines seen upon closer inspection. The binary masks  $V_i[s_j]$  indicate detected pixels being sufficiently affected whereas the right column depicts results with smooth edges.

magnified portions of sub-aperture images with apparent fringe artifacts in Figs. 10(a) and 10(d) as well as rectified counterparts exposing smooth edges in Figs. 10(c) and 10(f). Although the efficacy of our treatment is visually notable, this improvement does not present a huge impact on BRISQUE scores. This is likely due to the blind character of the metric and its unawareness of the hexagonal sampling artifact, which can be interpreted as reasonably high spatial frequencies. Another observation made in Fig. 10 is that organic object structures intentionally receive no treatment as they lack straight edges and are thus less affected.

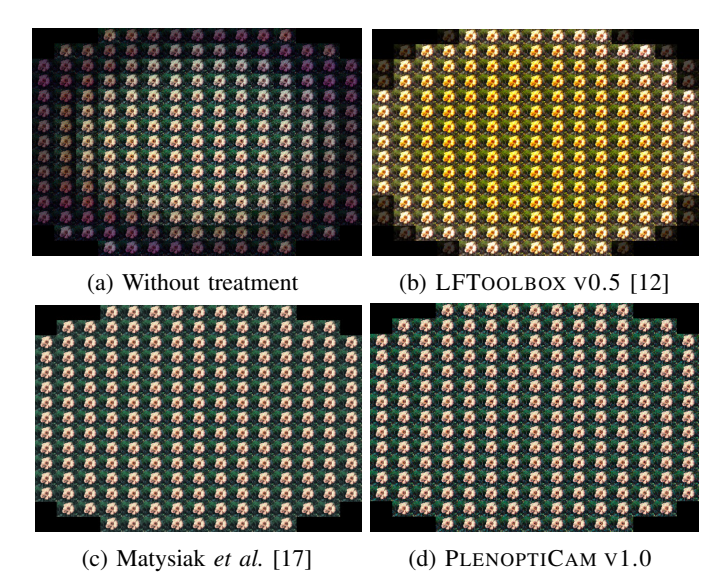


Fig. 11: Color equalization results with  $15 \times 15$  stitched sub-aperture images indicating illumination variances across a decomposed light-field. (a) our result without treatment, (b) Dansereau *et al.* [12], (c) GMM-based method [17] with 240 mins computation time and (d) our HM-MKL compound with 81 secs computation time.

Central sub-aperture images are not the only criterion to describe the quality of a light-field obtained from a plenoptic camera. For instance, rays arriving from non-paraxial angles suffer from natural vignetting causing color inconsistencies within a light-field which we aim to compensate for with the LFPCOLOREQUALIZER module. Figure 11 presents subaperture images stitched together for visual inspection of the light-field illumination variances before and after equalization treatment. For better visual analysis, sub-aperture images at a marginal position (i = 7, g = 2) are provided in Fig. 12.

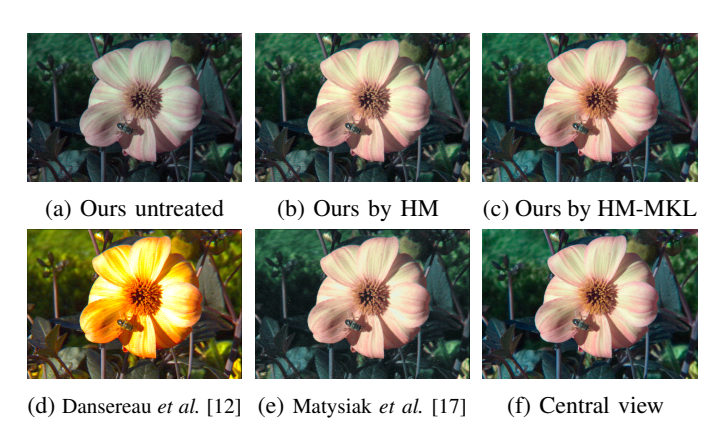


Fig. 12: Marginal view comparison of methods combating illumination fall-off at off-axis positions using an exemplary light-field image with M=15. The marginal view location is i = 7, g = 2 with (a) the untreated image, (b) after Histogram Matching (HM), (c) from the HM-MKL compound, (d) LFTOOLBOX V0.5 [12], (e) Matysiak et al. [17] and (f) the central sub-aperture image (i = 7, g = 7) as a reference.

For quantitative assessment of the color transfer we compute the average histogram distance denoted by D using the  $\ell^2$ norm as given by

$$D = ||f(E_c[s_i]) - f(E_q[s_i])||_2$$
(38)

where  $E_q[s_i]$  represents the marginal and  $E_c[s_i]$  the central sub-aperture image serving as the reference while  $f(\cdot)$  is the PDF from Eq. (26). Results of our color consistency measurements from Eq. (38) are depicted in Fig. 13.

Computation times of the different sub-aperture decomposition stages are given in Table II. The extensive computational load imposed by Matysiak's recoloring procedure [17] makes it impractical for us to iterate through an entire dataset.

TABLE II: Computation time comparison where M=15

Process	Dansereau et al.	Matysiak et al.	Ours
De-Multiplexing	70 secs	125 secs	325 secs
Hot Pixel Removal	not supported	100 secs	52 secs
Color Equalization	not supported	234 mins	81 secs
Total	70 secs	237 mins	458 secs

Using the afore-mentioned image metrics, no measurable improvements could be observed from rotating a plenoptic image. Nonetheless, rotation of the 4-D micro image representation proved to be more robust when processing large micro images (e.g. M=15) located at the image border. This is resolved by rotation as it shifts marginal micro images away

from the image border and enables consideration of marginal image pixels.

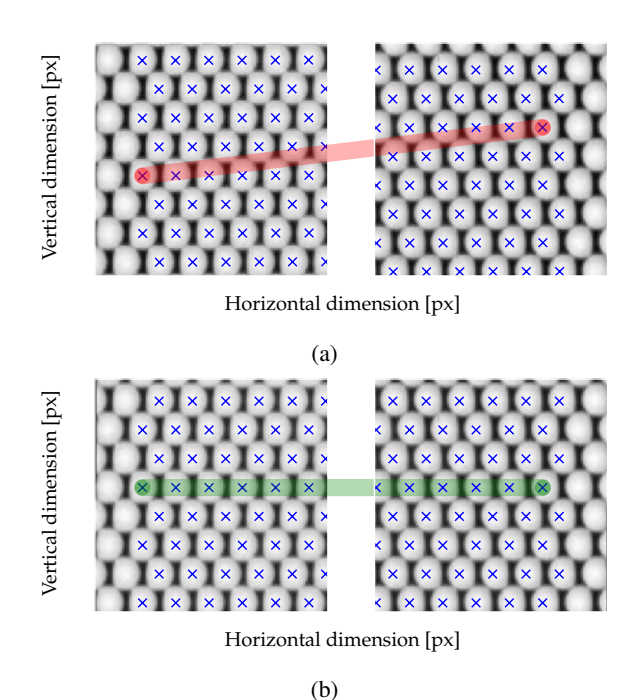
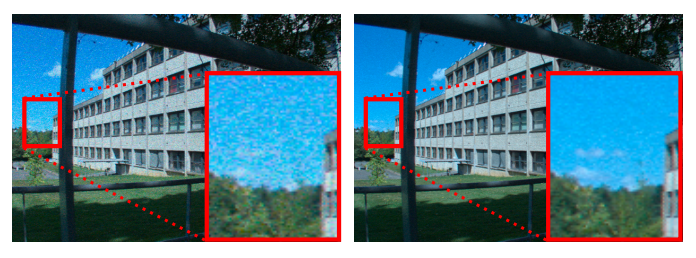


Fig. 14: Micro image array rotation with cropped views from a Lytro white image being untreated in (a) and rotated in (b). Transparent lines embrace MICs of the same row near image borders to demonstrate the effectiveness of the LFPROTATOR.

# C. De-Vignetting



(a) 74 dB PSNR from division (b) 85 dB PSNR from LSQ fit

Fig. 15: **De-vignetting** from a white image with Gaussian noise  $\sigma = 0.15$ . The noise was absent when de-vignetting the ground-truth. Noise propagates to the light-field during division as seen in (a) and is significantly suppressed in (b) via patch-wise micro image fitting based on Eqs. (16), (17) and (19). Our approach gains  $\sim 10 \text{ dB}$  of PSNR compared to the ordinary division as used by [12], [17].

Experimental validation of our LSQ-based de-vignetting in Eqs. (16), (17) and (19) is assessed using the Peak Signal-to-Noise-Ratio (PSNR) given by

$$PSNR = 20 \cdot \log_{10} \left( \frac{2^8 - 1}{\sqrt{\frac{1}{J} \sum_{j=1}^{J} (E_T[s_j] - E_c[s_j])^2}} \right) (39)$$

as a metric to analyse its effectiveness. For the ground-truth data  $E_T[s_i]$ , we use a photograph divided by a white image

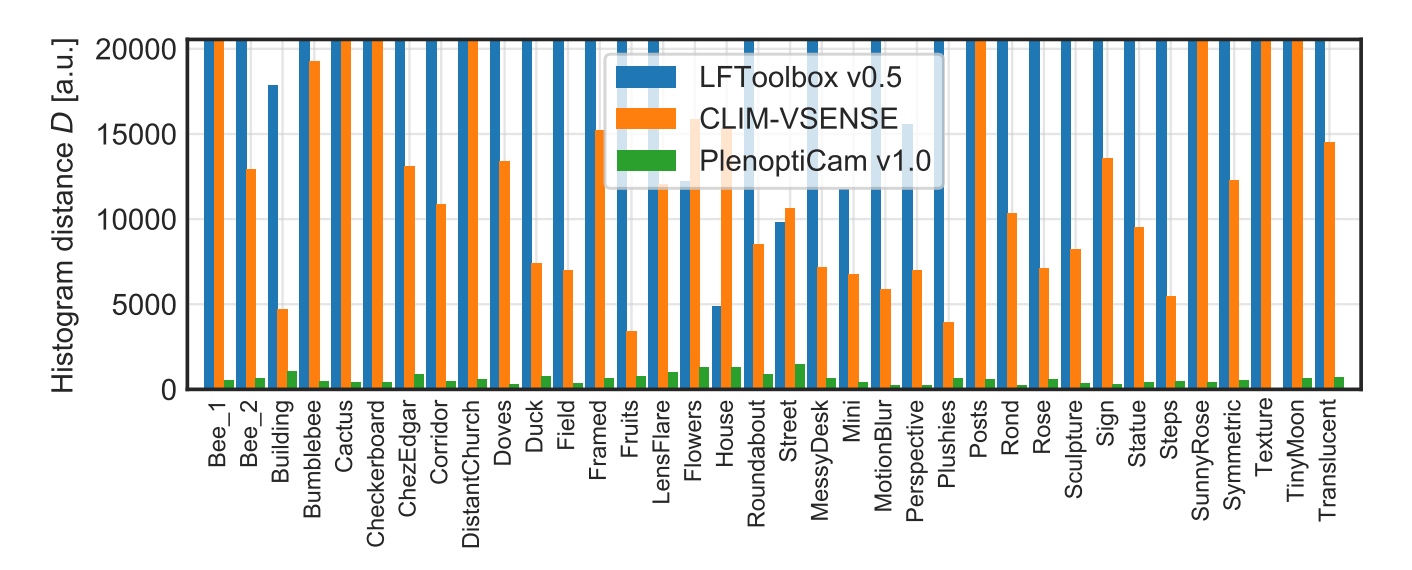


Fig. 13: Light-field color consistency metric from histogram distance D with low values indicating higher similarity between marginal views  $E_g[s_j]$  at position i = 7, g = 2 and corresponding central views  $E_c[s_j]$  in light-fields of size M = 15.

considered noiseless. This white image is then exposed to additive Gaussian noise with  $\sigma=0.15$  for de-vignetting by either classical division [12], [17] and our proposed fitting scheme. In doing so, we expect the synthetic noise to propagate during de-vignetting, however, with sufficient suppression (i.e. higher PSNR) for our LSQ approach. The results in Fig. 15 show that our method retains the image quality by gaining  $\sim 10~\mathrm{dB}$  of dynamic range with respect to noise. This is a consequence of the least-squares fit treating pixel noise as residuals. Although our evaluation contains highly amplified noise, this method is regarded equally beneficial for low-noise images.

# D. Refocusing

For the refocusing assessment, we compare the proposed LFPREFOCUSER module against LYTRO POWER TOOLS V1.0. Refocused images are depicted in Fig. 16. We choose the *Bumblebee.lfp* image from the IRISA dataset [36] as it exhibits organic object structures spread through a wide range of depth.

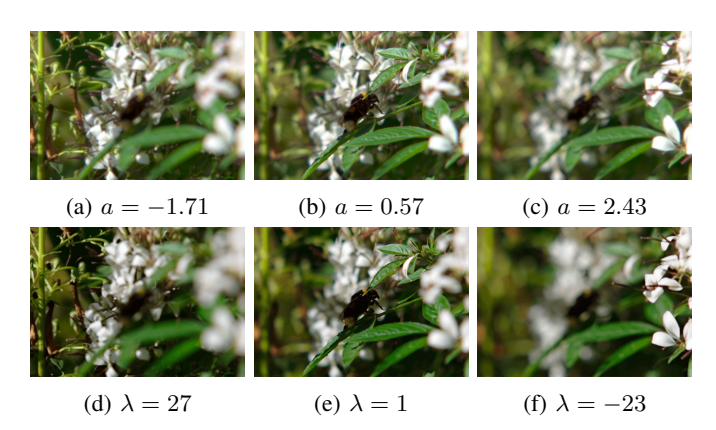


Fig. 16: **Refocused photographs** from PLENOPTICAM V1.0 in the top row with shift and sum parameter a in comparison to results processed by LYTRO POWER TOOLS V1.0 in the bottom row with focus parameter  $\lambda$ .

Quantitative comparison is achieved by analysis of the sharpness and BRISQUE score of local image details. For the sharpness analysis, we follow the Mavridaki and Mezaris [42] approach by transforming cropped versions of a refocused image slice  $E_a''[s_j,t_h]$  to the Fourier domain using the Discrete Fourier Transformation (DFT) and extracting the magnitude signal  $\mathcal{X}\left[\sigma_{\omega},\rho_{\psi}\right]$  by

$$\mathcal{X}\left[\sigma_{\omega},\,\rho_{\psi}\right] = \left|\sum_{j=\xi}^{\Xi} \sum_{h=\varpi}^{\Pi} E_{a}^{"}\left[s_{j},\,t_{h}\right]\right| \tag{40}$$

$$\exp\left(-2\pi\kappa(j\omega/(\Xi-\xi)+h\psi/(\Pi-\varpi))\right)$$

where  $\kappa = \sqrt{-1}$  and  $|\cdot|$  yields absolute values. Given the 2-D magnitude signal  $\mathcal{X} [\sigma_{\omega}, \rho_{\psi}]$ , the total energy TE reads

$$TE = \sum_{\omega=1}^{\Omega} \sum_{\psi=1}^{\Psi} \mathcal{X} \left[ \sigma_{\omega} , \rho_{\psi} \right]^{2}$$
 (41)

where  $\Omega = \lceil (\Xi - \xi)/2 \rceil$  and  $\Psi = \lceil (\Pi - \varpi)/2 \rceil$  are borders cropping the first quarter of the unshifted magnitude signal. To isolate the energy of high frequency elements HE, we compute the power of low frequencies and subtract them from TE which reads

$$HE = TE - \sum_{\omega=1}^{Q_H} \sum_{\psi=1}^{Q_V} \mathcal{X} \left[ \sigma_{\omega} , \rho_{\psi} \right]^2$$
 (42)

with  $Q_H$  and  $Q_V$  as scalar limits in the range of  $\{1,2,\ldots,\Omega\}$  and  $\{1,2,\ldots,\Psi\}$  separating low from high frequencies. In our experiments we set the limits to a five hundredths of the cropped image resolution. Finally, the sharpness S is a frequency ratio of refocused image portions obtained by

$$S = \frac{HE}{TE} \tag{43}$$

which serves as our blur metric.

From the cropped view of the Lytro image in Fig. 17(1), it is seen that there is no gradual decrease in blur between objects at different depth leading to an unnatural appearance of image blur. Images rendered with LFPREFOCUSER do not expose such sudden change in sharpness. It is only up to speculation on how Lytro's refocusing algorithm works. The high resolution and occasional blur artifacts around object edges suggest that Lytro super-resolves images at the first stage and then re-blurs spatial areas guided by a previously computed depth map. This may explain blur artifacts at object boundaries, which rely on the quality of a depth map.

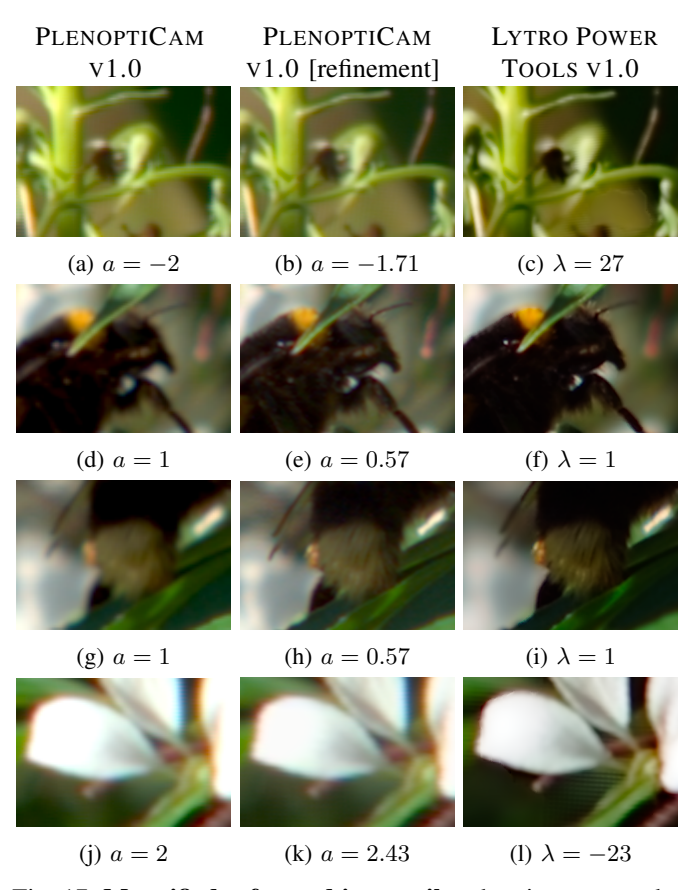


Fig. 17: **Magnified refocused image tiles** showing texture details which are quantified by our blur metric S in Table III. The left and middle column contain results from PLENOPTICAM V1.0 whereas (b), (e), (h), (k) are rendered with sub-pixel precision. The right column is obtained from LYTRO POWER TOOLS V1.0 using focus parameter  $\lambda$ .

TABLE III: Metric assessment of refocused images

Fig. 17 Metrics	(a)	(b)	(c)	(d)	(e)	(f)
Sharpness S	0.034	0.040	0.060	0.107	0.107	0.224
BRISQUE score	84.29	83.51	81.67	92.43	81.29	77.29
Fig. 17 Metrics	(g)	(h)	(i)	(j)	(k)	(1)
Sharpness S	0.107	0.107	0.125	0.022	0.027	0.054
BRISQUE score	92.43	81.29	81.19	94.30	90.56	80.22

It is therefore questionable whether the measured sharpness in Lytro's refocus algorithm arises from high frequency artifacts. By visual inspection, however, it becomes apparent that the magnified views from Lytro expose more image detail at small  $\lambda$  value. This observation is backed by respective scores from the BRISQUE metric in Table III. On the contrary, occasional artifact patterns as in Fig. 17(1) may still appeal unpleasant to the human visual perception.

An exemplary result of the LFPSCHEIMPFLUG rendering engine is depicted in Fig. 18. Note how image areas in the upper left background expose sharp details, whereas the focus gradually moves toward the lower right foreground. This is a consequence of the synthetic focus plane being tilted with respect to the image sensor.



Fig. 18: Scheimpflug rendered photograph from LFP-SCHEIMPFLUG class with  $a = \{0, 1\}$  and sub-pixel precision.

# IV. CONCLUSIONS

Plenoptic image decomposition is a crucial task in light-field rendering for which we propose a pipeline with outstanding image quality. To the best of our knowledge, PLENOPTICAM is the only framework that allows users to automatically calibrate footage from different types of plenoptic cameras regardless of the micro lens specification. We achieve this by employing blob detection, non-maximum suppression and a generic MLA grid geometry recognition. The light-field color equalization stage is taken to a new level by using histogram matching in conjunction with a Monge-Kantorovich solver to yield convincing quantitative results at reasonable computation times, which accelerates a previous method based on Gaussian Mixture Models (GMM) by several orders of magnitude. For plenoptic image alignment, we created an alternative element-wise micro image resampling procedure. Moreover, we are first to address fringe artifacts caused by hexagonal micro lens arrangements, which are successfully reduced by our novel identification scheme. An extensive quantitative assessment of state-of-the-art sub-aperture image decomposition pipelines has been carried out in this paper with the result of outperforming other tool chains in two thirds of the cases, using a wide range of image metrics such as BRISQUE, average histogram distance via  $\ell^2$  norm and a blur metric.

These findings and respective implementations are released as an open-source software framework made available as a repository on GitHub [43] to allow others to participate and contribute. The herein presented framework is intended to disburden newcomers and facilitate first steps in the field of plenoptic imaging. Peers are encouraged to report bugs and actively expand this software. PLENOPTICAM may lay the groundwork for future algorithm development and testing of plenoptic data.

Such extensions may include, but are not limited to, an algorithm development for the focused plenoptic camera as initially discovered by Lumsdaine and Georgiev [44]. An implementation of a super-resolution technique may be accomplished on the basis of early pioneering work [45], [40]. It should also be feasible to enhance the image quality by combating optical aberrations as shown in previous studies [46], [47], [48], [41], [49] or by making use of the Bayer demosaicing similar to what Yu and Yu have revealed [50]. Until now, rectification for lens distortions exceeded the scope as this can be accomplished using traditional computer vision libraries. However, correct disparity estimation requires counteracting distortions in sub-aperture images at a preceding stage.

We believe that our work will be a substantial contribution to the field of plenoptic cameras, which is not limited to the image processing community. As Dansereau's LFTOOLBOX has shown, there is a large group of researchers experimenting with plenoptic cameras demonstrating the demand for an easy-to-use software addressing the special requirements for plenoptic imaging. PLENOPTICAM may serve this broad user group including image scientists, programmers in the fields of data science, medical and industrial engineering or photography independent of the user's operating system. In particular, PLENOPTICAM facilitates light-field data preparation for visual machine learning systems such as convolutional neural networks, which currently receive an increasing interest from a variety of scientific and industrial communities. The chosen open source license model enables cost-free usage and code republication with modifications, giving users the opportunity to extend the presented software.

#### REFERENCES

- R. Ng, M. Levoy, M. Brèdif, G. Duval, M. Horowitz, and P. Hanrahan, "Light field photography with a hand-held plenoptic camera," Stanford University, Tech. Rep. CTSR 2005-02, 2005.
- [2] C. Hahne, A. Aggoun, V. Velisavljevic, S. Fiebig, and M. Pesch, "Refocusing distance of a standard plenoptic camera," *Opt. Express*, vol. 24, no. 19, pp. 21521–21540, Sep 2016. [Online]. Available: http://www.opticsexpress.org/abstract.cfm?URI=oe-24-19-21521
- [3] R. Prevedel, Y.-G. Yoon, M. Hoffmann, N. Pak, G. Wetzstein, S. Kato, T. Schrödel, R. Raskar, M. Zimmer, E. S. Boyden *et al.*, "Simultaneous whole-animal 3d imaging of neuronal activity using light-field microscopy," *Nature methods*, vol. 11, no. 7, p. 727, 2014.
- [4] H. Li, C. Guo, D. Kim-Holzapfel, W. Li, Y. Altshuller, B. Schroeder, W. Liu, Y. Meng, J. French, K.-I. Takamaru, M. Frohman, and S. Jia, "Fast, volumetric live-cell imaging using high-resolution light-field microscopy," bioRxiv, 2018. [Online]. Available: https://www.biorxiv.org/content/early/2018/10/10/439315
- [5] N. Bedard, T. Shope, A. Hoberman, M. Ann Haralam, N. Shaikh, J. Kovačević, N. Balram, and I. Tošić, "Light field otoscope design for 3d in vivo imaging of the middle ear," *Biomedical Optics Express*, vol. 8, p. 260, 01 2017.
- [6] D. W. Palmer, T. Coppin, K. Rana, D. G. Dansereau, M. Suheimat, M. Maynard, D. A. Atchison, J. Roberts, R. Crawford, and A. Jaiprakash, "Glare-free retinal imaging using a portable light field fundus camera," *Biomedical Optics Express*, vol. 9, p. 3178, 07 2018.

- [7] P. P. Srinivasan, T. Wang, A. Sreelal, R. Ramamoorthi, and R. Ng, "Learning to synthesize a 4d rgbd light field from a single image," in The IEEE International Conference on Computer Vision (ICCV), Oct 2017
- [8] M. Levoy and P. Hanrahan, "Light field rendering," Stanford University, Tech. Rep., 1996.
- [9] E. H. Adelson and J. Y. Wang, "Single lens stereo with a plenoptic camera," *IEEE Transactions on Pattern Analysis and Machine Intelligence*, vol. 14, no. 2, pp. 99–106, February 1992.
- [10] C. Hahne, A. Aggoun, V. Velisavljevic, S. Fiebig, and M. Pesch, "Baseline and triangulation geometry in a standard plenoptic camera," *International Journal of Computer Vision*, vol. 126, no. 1, pp. 21–35, Jan 2018. [Online]. Available: https://doi.org/10.1007/s11263-017-1036-4
- [11] D. Cho, M. Lee, S. Kim, and Y.-W. Tai, "Modeling the calibration pipeline of the lytro camera for high quality light-field image reconstruction," in *IEEE International Conference on Computer Vision (ICCV)*, December 2013, pp. 3280–3287.
- [12] D. G. Dansereau, O. Pizarro, and S. B. Williams, "Decoding, calibration and rectification for lenselet-based plenoptic cameras," in *IEEE Interna*tional Conference on Computer Vision and Pattern Recognition (CVPR), June 2013, pp. 1027–1034.
- [13] N. Patel, "Ifptools," https://github.com/nrpatel/Ifptools, 2011.
- [14] B. Esfahbod, "python-lfp-reader," https://github.com/behnam/python-lfp-reader, 2013.
- [15] Y. Bok, H.-G. Jeon, and I. S. Kweon, "Geometric calibration of microlens-based light-field cameras using line features," in *Proceedings of European Conference on Computer Vision (ECCV)*, 2014.
- [16] P. David, M. Le Pendu, and C. Guillemot, "White lenslet image guided demosaicing for plenoptic cameras," 10 2017, pp. 1–6.
- [17] P. Matysiak, M. Grogan, M. L. Pendu, M. Alain, and A. Smolic, "A pipeline for lenslet light field quality enhancement," 2018 25th IEEE International Conference on Image Processing (ICIP), Oct 2018. [Online]. Available: http://dx.doi.org/10.1109/ICIP.2018.8451544
- [18] C. Hahne and A. Aggoun, "Plenoptisign: An optical design tool for plenoptic imaging," *SoftwareX*, vol. 10, p. 100259, 2019. [Online]. Available: http://www.sciencedirect.com/science/article/pii/ S2352711019300159
- [19] T. Lindeberg, Scale-Space Theory in Computer Vision, 01 1994.
- [20] J. L. Crowley, O. Riff, and J. H. Piater, "Fast computation of characteristic scale using a half-octave pyramid," in In: Scale Space 03: 4th International Conference on Scale-Space theories in Computer Vision, Isle of Skye, 2002.
- [21] C.-K. Liang and Z. Wang, "Calibration of light-field camera geometry via robust fitting," U.S. Patent 9 420 276 B2, Aug. 2016.
- [22] T. Q. Pham, "Non-maximum suppression using fewer than two comparisons per pixel," in *Advanced Concepts for Intelligent Vision Systems*, J. Blanc-Talon, D. Bone, W. Philips, D. Popescu, and P. Scheunders, Eds. Berlin, Heidelberg: Springer Berlin Heidelberg, 2010, pp. 438–451.
- [23] J. J. Moré, "The levenberg-marquardt algorithm: Implementation and theory," in *Numerical Analysis*, G. A. Watson, Ed. Berlin, Heidelberg: Springer Berlin Heidelberg, 1978, pp. 105–116.
- [24] A. Kordecki, H. Palus, and A. Bal, "Practical vignetting correction method for digital camera with measurement of surface luminance distribution," Signal, Image and Video Processing, vol. 10, pp. 1417— -1424, 2016.
- [25] D. Menon, S. Andriani, and G. Calvagno, "Demosaicing With Directional Filtering and a posteriori Decision," *IEEE Transactions on Image Processing*, vol. 16, no. 1, pp. 132–141, jan 2007. [Online]. Available: http://ieeexplore.ieee.org/document/4032820/
- [26] M. Seifi, N. Sabater, V. Drazic, and P. Perez, "Disparity-guided demosaicking of light field images," 10 2014.
- [27] Y. Li and M. Sjöström, "Depth-assisted demosaicing for light field data in layered object space," in 2019 IEEE International Conference on Image Processing (ICIP), 2019, pp. 3746–3750.
- [28] F. Pitié and A. Kokaram, "The linear monge-kantorovitch colour mapping for example-based colour transfer," *IET Conference Proceedings*, pp. 23–23(1), January 2007.
- [29] R. Gonzalez and R. Woods, Digital Image Processing, Global Edition. Pearson. 2017.
- [30] F. Pitié, A. Kokaram, and R. Dahyot, ser. Image Processing Series. CRC Press, Sep 2008, ch. Enhancement of Digital Photographs Using Color Transfer Techniques, pp. 295–321, 0. [Online]. Available: http://dx.doi.org/10.1201/9781420054538.ch11
- [31] A. Isaksen, "Dynamically reparameterized light fields," Master's thesis, Electrical Engineering and Computer Science, Massachusetts Institute of Technology, November 2000.

- [32] C. Hahne, A. Lumsdaine, A. Aggoun, and V. Velisavljevic, "Real-time refocusing using an fpga-based standard plenoptic camera," *IEEE Transactions on Industrial Electronics*, vol. 65, no. 12, pp. 9757–9766, Dec 2018.
- [33] M. Schambach and F. Puente León, "Microlens array grid estimation, light field decoding, and calibration," *IEEE transactions on computa*tional imaging, vol. 6, p. 591–603, 2020.
- [34] C. Pitts, T. Knight, C. Liang, and Y. Ng, "Compensating for variation in microlens position during light-field image processing," August 2013, uS Patent App. 13/774,971. [Online]. Available: http://www.google.co.uk/patents/US20130222606
- [35] L. Mignard-Debise and I. Ihrke, "A Vignetting Model for Light Field Cameras with an Application to Light Field Microscopy," *IEEE Transactions on Computational Imaging*, p. 10, Apr. 2019. [Online]. Available: https://hal.archives-ouvertes.fr/hal-02263377
- [36] R. C. Daudt and C. Guillemot. Lytro illum light field dataset. [Online]. Available: https://www.irisa.fr/temics/demos/IllumDatasetLF/index.html
- [37] A. Mittal, A. K. Moorthy, and A. Bovik, "No-reference image quality assessment in the spatial domain," *IEEE Transactions on Image Pro*cessing, vol. 21, pp. 4695–4708, 2012.
- [38] Bukalapak, "Pybrisque," https://github.com/bukalapak/pybrisque, 2020.
- [39] D. G. Dansereau, O. Pizarro, and S. B. Williams, "Linear volumetric focus for light field cameras," ACM Trans. Graph., vol. 34, no. 2, pp. 15:1–15:20, Mar. 2015. [Online]. Available: http://doi.acm.org/10.1145/2665074
- [40] C.-K. Liang and R. Ramamoorthi, "A light transport framework for lenslet light field cameras," ACM Trans. Graph., vol. 34, no. 2, Mar. 2015. [Online]. Available: https://doi.org/10.1145/2665075
- [41] L.-Y. Wei, C.-K. Liang, G. Myhre, C. Pitts, and K. Akeley, "Improving light field camera sample design with irregularity and aberration," ACM Trans. Graph., vol. 34, no. 4, Jul. 2015. [Online]. Available: https://doi.org/10.1145/2766885
- [42] E. Mavridaki and V. Mezaris, "No-reference blur assessment in natural images using fourier transform and spatial pyramids," in 2014 IEEE International Conference on Image Processing (ICIP), October 2014, pp. 566–570.
- [43] C. Hahne, "Plenopticam," https://github.com/hahnec/plenopticam, 2020.
- [44] A. Lumsdaine and T. Georgiev, "Full resolution lightfield rendering," Adobe Systems, Inc., Tech. Rep., January 2008.
- [45] T. E. Bishop, S. Zanetti, and P. Favaro, "Light field superresolution," in IEEE International Conference on Computational Photography (ICCP), 2009.
- [46] R. Ng, "Digital light field photography," Ph.D. dissertation, Stanford University, July 2006.
- [47] R. Ng and P. Hanrahan, "Digital correction of lens aberrations in light field photography," in *International Optical Design Conference*, vol. Proc. SPIE 6342. Stanford University, July 2006. [Online]. Available: http://dx.doi.org/10.1117/12.692290
- [48] N. Cohen, S. Yang, A. Andalman, M. Broxton, L. Grosenick, K. Deisseroth, M. Horowitz, and M. Levoy, "Enhancing the performance of the light field microscope using wavefront coding," *Opt. Express*, vol. 22, no. 20, pp. 24817–24839, Oct 2014. [Online]. Available: http://www.opticsexpress.org/abstract.cfm?URI=oe-22-20-24817
- [49] C.-K. Liang, C. Pitts, C. Craddock, and G. Myhre, "Light-field aberration correction," U.S. Patent 9 628 684 B2, Apr. 2017.
- [50] Z. Yu, J. Yu, A. Lumsdaine, and T. Georgiev, "An analysis of color demosaicing in plenoptic cameras," in *IEEE International Conference* on Computer Vision and Pattern Recognition (CVPR), 2012, pp. 901– 908.

# APPENDIX A SCALE SPACE THEOREM

**Theorem** M and  $\sigma^*$  are equal up to scale in Eqs. (1) and (3). *Proof.* Let  $G(\sigma, \mathbf{x})$  be a Gaussian function of  $\mathbf{x} = \{x, y\} \in \mathbb{R}^2$  and  $\sigma$  the scale in a Laplacian pyramid with blob radius r, then

$$G(\sigma, x, y) = e^{-\frac{x^2 + y^2}{2\sigma^2}}$$

$$\partial_x G(\sigma, x, y) = -\frac{x}{\sigma^2} e^{-\frac{x^2 + y^2}{2\sigma^2}}$$

$$\partial_{xx} G(\sigma, x, y) = -\frac{1}{\sigma^2} e^{-\frac{x^2 + y^2}{2\sigma^2}} + \frac{x^2}{\sigma^4} e^{-\frac{x^2 + y^2}{2\sigma^2}}$$

$$\nabla^2 G(\sigma, x, y) = \partial_{xx} G(\sigma, x, y) + \partial_{yy} G(\sigma, x, y)$$

$$= \left(\frac{x^2 + y^2}{\sigma^4} - \frac{2}{\sigma^2}\right) e^{-\frac{x^2 + y^2}{2\sigma^2}}$$

$$r^2 = x^2 + y^2$$

$$0 = \frac{r^2}{\sigma^4} - \frac{2}{\sigma^2}$$

$$r^2 = 2\sigma^2$$

$$r = \sqrt{2}\sigma$$

$$M \approx 2r = 2\sqrt{2}\sigma$$



Christopher Hahne is a visiting scholar affiliated with the School of Mathematics and Computer Science at the University of Wolverhampton. He received the B.Sc. degree in Media Technology in 2012 from the University of Applied Sciences Hamburg while working at R&D departments of Rohde & Schwarz as well as the ARRI Group. After becoming a visiting student at Brunel University in 2012, he started an M.Phil. and transferred to a bursary-funded Ph.D. programme at the University of Bedfordshire together with his supervisor Prof.

Amar Aggoun. Upon completion of his doctoral studies, he published 10 high impact peer-reviewed journal and conference articles, most of them written as the main author. In his professional career, he has worked for trinamiX GmbH (BASF SE) and Pepperl+Fuchs SE, which led to 2 granted patents. His research interests concentrate on algorithm development in the fields of computer vision, audio processing and depth sensing.



Amar Aggoun is currently the Head of School of Mathematics and Computer Science and Professor of Visual Computing at the University of Wolverhampton. He received the "Ingenieur d'état" degree in Electronics Engineering in 1986 from Ecole Nationale Polytechnique d'Alger in (Algiers, Algeria) and a PhD degree in Electronic Engineering from the University of Nottingham. His academic career started at the University of Nottingham where he held the positions of research fellow in low power DSP architectures and visiting lecturer in Electronic

Engineering and Mathematics. In 1993 he joined De Montfort University as a lecturer and progressed to the position of Principal Lecturer in 2000. In 2005 he joined Brunel University as Reader in Information and Communication Technologies. From 2013 to 2016, he was at the University of Bedfordshire as Head of School of Computer Science and Technology. He was also the director of the Institute for Research in Applicable Computing which oversees all the research within the School. His research is mainly focused on 3D Imaging and Immersive Technologies and he successfully secured and delivered research contracts worth in excess of £6.9M, funded by the research councils UK, Innovate UK, the European commission and industry. Amongst the successful project, he was the initiator and the principal coordinator and manager of a project sponsored by the EU-FP7 ICT-4-1.5-Networked Media and 3D Internet, namely Live Immerse Video-Audio Interactive Multimedia (3D VIVANT). He holds three filed patents, published more than 200 peerreviewed journals and conference publications and contributed to two white papers for the European Commission on the Future Internet. He also served as Associate Editor for the IEEE/OSA Journal of Display Technologies.